•机械工程•

DOI:10.12454/j.jsuese.202300783

本刊网刊

面向无磁钻具表面强化的Ni60合金激光熔覆工艺研究

刘丽兰[1],李思聪[1],杨　帆[1],韩飞燕[2],吴子英[1]

(1.西安理工大学 机械与精密仪器工程学院,陕西 西安 710048;2.西安航空职业技术学院 航空制造工程学院,陕西 西安 710089)

摘　要:无磁钻具材料为316L不锈钢,在其表面激光熔覆高硬质合金可有效提高耐磨耐蚀性。采用激光同轴送粉技术在316L不锈钢表面熔覆Ni60合金粉末,以激光功率、扫描速度和送粉速率为影响因素,开展激光熔覆正交试验。首先,进行3因素4水平的单层单道激光熔覆试验,根据所制备的16组熔覆层的裂纹密度、稀释率和成形系数筛选出8组无裂纹熔覆层的工艺参数;再以显微硬度、稀释率和成形系数为质量评价指标,提出了综合加权赋分的方法并优选出3组工艺参数;最后,采用优选出的工艺参数在50%搭接率下进行单层多道激光熔覆试验。通过熔覆层横截面形貌分析可知,单层多道熔覆层均在首道出现较高的稀释率,后继道数的稀释率降低并趋于平稳,成形良好的熔覆层的稀释率在15%～20%。通过熔覆层横截面显微硬度测量可知,单层多道熔覆层硬度略高于单层单道熔覆层,前者熔覆层横截面的显微硬度是基体硬度的4倍左右。通过观察单层多道熔覆层横截面显微金相组织发现,熔覆层从结合区到表面,组织形态呈现出从连续平面晶、树枝晶到等轴晶的转变,成形良好,无明显气孔、裂纹等缺陷。最后,根据熔覆层金相组织和几何形貌确定了满足无磁发射短节熔覆层要求的最佳工艺参数。所得结论为后续井下无磁钻具服役环境下的Ni60熔覆层摩擦磨损性能研究奠定了基础。

关键词:无磁钻具;Ni60合金;综合加权赋分;工艺优化

中图分类号:TG174　　**文献标志码:**A　　**文章编号:**2096-3246(2025)04-0303-10

近钻头随钻测量仪器是实现地质导向钻井技术的重要物理载体,能在近钻头部位测量钻压、扭矩及井下环空压力等参数。无磁钻具是保护随钻测量仪器内部电子元件的重要结构[1],含有多个短节体,其材质均为无磁316L不锈钢,耐磨耐蚀性较差[2]。在定向钻井施工过程中,由于高温、高压和高硬地质的恶劣工况,无磁钻具磨损问题日益突出[3]。无磁钻具表面一旦受到剧烈磨损发生破坏,将无法有效保护其内部的电子测量元件,造成测量数据出现误差甚至仪器失效。对无磁钻具进行防磨处理,增加其耐磨性,可以延长使用寿命[4]。

激光熔覆是一种高生产率、低污染的绿色再制造技术,在提高基体材料表面耐磨性方面有显著效果[5–7],已被广泛应用于航空航天、汽车、矿山机械和石油化工等领域[8–10]。随钻测量仪造价昂贵,维修周期长并且维修费用高,采用激光熔覆增材抗磨技术在无磁钻具表面易受磨损部位形成高硬质合金耐磨带涂层以提高其耐磨耐蚀能力是十分必要的,这也是目前地质导向钻井技术研究的热点[11–12]及重点方向[13–14]。Stelcar65镍基粉末含有大量的碳化钨,用其制造的涂层具有很高的耐磨耐腐蚀性[15],在石化领域多用于石油钻头及钻柱的表面强化,但它的粉末价格高且粉末利用率较低。比较而言,Ni60镍基合金粉末同样具有高硬度和高耐磨耐蚀性能[16–17],而价格约为Stelcar65价格的1/3,若将该合金粉末大范围应用于无磁钻具的激光熔覆,可节约大量经济成本,创造更大经济效益。但Ni60合金粉末熔覆的最大缺点是裂纹敏度较高[18–19],严重制约了其工程应用的广泛性。熔覆层质量优劣的关键在于激光熔覆工艺参数的调控,如何设计并确定适合Ni60合金粉末激光熔覆的工艺参数是目前亟需解决的关键问题。

目前,针对镍基合金激光熔覆的工艺研究,众多学者已经做了大量的工作。吴祖鹏等[20]研究了针对Ni60A合金激光熔覆裂纹消除方法,提出采用预热

收稿日期:2023－10－06　　**修回日期:**2024－01－25　　**网络出版日期:**2024－06－03

基金项目:国家自然科学基金项目(42472381)

作者简介:刘丽兰(1979—),女,副教授,博士. 研究方向:机械系统摩擦磨损及激光熔覆加工. E-mail: liulilans@163.com

保温工艺能有效的降低熔覆层温度梯度，进而减少熔覆层的裂纹敏感性。李琦等[21]进行了Ni基合金激光熔覆层裂纹机理研究，得出熔覆层材料与基体材料物性差异导致的热应力达到材料的断裂强度时，熔覆层极易发生脆性断裂，产生宏观裂纹并扩展。王永东等[22]在35CrMnSi钢基体表面制备不同激光熔覆工艺参数的Ni60A熔覆层，研究了不同激光熔覆工艺参数下Ni60A熔覆层的组织与性能。Wu等[23]在A3钢板上制备了Ni60A粉末+25%WC合金熔覆层（25%WC表示碳化钨质量分数为25%），采用响应面法对熔覆工艺参数进行了优化，结果表明，激光熔覆工艺参数对稀释率的影响比对涂层单位有效面积的影响更加显著。Liu等[24]提出了一种基于响应面法的多目标优化方法来获得最优的激光熔覆工艺参数，并在预热的铜合金基材上实现了镍基合金粉末涂层制备。黄海博等[19]在45钢基材上熔覆了Ni60合金粉末，通过设计正交试验分析激光功率送粉量扫描速率对裂纹产生的影响，找出了最优工艺参量。史亚盟等[25]为提高饲草揉切机中揉切刀片的耐磨性，采用激光熔覆技术在65Mn钢表面制备Ni60a/SiC复合粉末熔覆层，分析镀层了的显微硬度、物相组成和摩擦磨损性能，得到最佳激光熔覆工艺参数组合。史强等[26]采用高速激光熔覆系统在破碎机锤头中常用的材料高锰钢表面制备了Ni60耐磨熔覆层，通过正交试验极差分析优化得到了最佳工艺参数。Wang等[27]采用电磁辅助激光熔覆方法在纯铁基体上制备了Ni60合金涂层，分析了合金涂层的组织和性能。

本文针对无磁钻具表面激光熔覆Ni60合金粉末增材强化的工艺优化问题，结合正交试验，提出以熔覆层稀释率、成形系数和显微硬度综合加权赋分的方法，获得在316L不锈钢基材上制备无裂纹Ni60合金涂层的最优工艺参数。对熔覆层的着色探伤、金相组织和显微硬度分析表明，所制备的合金涂层冶金结合致密，表面强化效果明显。研究成果为后续井下服役条件下的Ni60熔覆层摩擦磨损性能研究奠定了基础。

1 试　验

无磁发射短节是井下无磁钻具组合的一个关键零件，激光熔覆的要求为：单层熔覆，熔覆层厚度为2.0～2.5 mm，熔覆层维氏硬度在580～630 HV。当在没有预研工艺的情况下初步进行激光熔覆Ni60合金粉末时，根据经验设置激光熔覆各项工艺参数，裂纹结果短节表面熔覆层出现了大量裂纹并逐渐剥落，裂纹如图1所示。该现象产生的主要原因是工艺参数选取不合理。因此，为了成功在316L不锈钢基体上制备无裂纹Ni60合金涂层，本文开展Ni60合金粉末激光熔覆工艺参数研究。

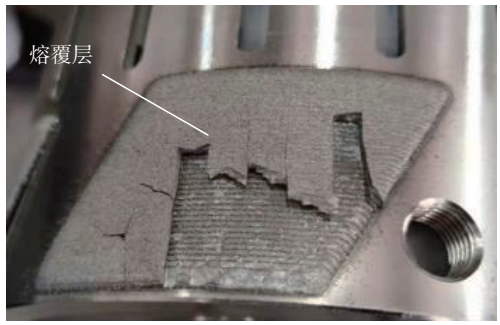

图1　发射短节熔覆层裂纹

Fig. 1　Cracks in the coating of the emission short

1.1　试验平台及材料

试验设备主要包括KUKA六轴机械臂、同轴光纤激光熔覆头、LDF–3000–60型半导体激光器及RC–PGF–D智能型气载式送粉器，激光熔覆试验平台见图2。熔覆层材料为Ni60合金粉末，成分见表1。表1中，Bal表示其余的全部质量分数。基体材料为316L不锈钢，成分见表2。基材尺寸为200 mm×100 mm×10 mm；试验前使用砂纸对基材表面进行充分打磨，再用无水乙醇清洗基体表面，去除基体表面油污、杂质颗粒等。基材底部放置隔热板，以降低熔覆层及基体的冷却速率。

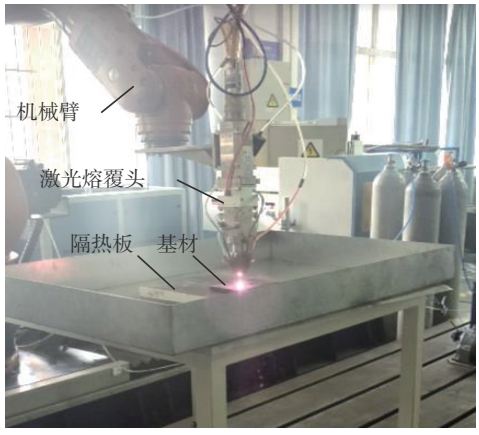

图2　激光熔覆试验平台

Fig. 2　Laser cladding experimental platform

表1　316L不锈钢化学成分

Tab. 1　Chemical composition of 316L

%

元素	质量百分比	元素	质量百分比
C	0.080	Cr	16.000～18.000
Si	1.000	Mo	2.000～3.000
Mn	2.000	S	<0.002
P	0.045	Fe	Bal
Ni	12.000～14.000		

表2　Ni60合金粉末化学成分

Tab. 2　Chemical composition of Ni60 alloy powder

%

元素	质量百分比	元素	质量百分比
C	0.8	B	3.0
Si	4.0	Cr	15.5
Fe	15.0	Ni	Bal

1.2　试验方法

设计Ni60合金粉末单层单道激光熔覆正交试验，熔覆长度为40 mm。选定激光功率P、扫描速度V_s和送粉速率V_t共计3个参数作为影响因素，每个因素设置4个水平，采用L16(3^4，3因素4水平)型正交表设计试验方案，获得16组工艺参数，具体方案见表3。

表3　正交试验参数

Tab. 3　Orthogonal test parameters

编号	激光功率P/W	扫描速度V_s/(mm·s^{-1})	送粉速率V_t/(r·min^{-1})
A1	1 400	3	0.4
A2	1 400	4	0.6
A3	1 400	5	0.8
A4	1 400	6	1.0
A5	1 600	3	0.6
A6	1 600	4	0.4
A7	1 600	5	1.0
A8	1 600	6	0.8
A9	1 800	3	0.8
A10	1 800	4	1.0
A11	1 800	5	0.4
A12	1 800	6	0.6
A13	2 000	3	1.0
A14	2 000	4	0.8
A15	2 000	5	0.6
A16	2 000	6	0.4

按照表3工艺参数进行激光熔覆试验获得16道熔覆层，采用渗透探伤检测熔覆层是否出现裂纹，然后使用线切割机床切割熔覆层横截面，并采用浓度为4%的硝酸酒精腐蚀，利用倒置系统金相显微镜观察熔覆层横截面金相组织。使用显微维氏硬度计测量熔覆层横截面的微观硬度，试验参数：载荷为500 g，加载时间15 s，测量间距0.15 mm。

根据试验结果，测量熔覆层几何尺寸，计算质量评价参数，筛选出无裂纹且稀释率合适的熔覆层，再采用综合加权赋分方法，将显微硬度、稀释率和成形系数进行综合评定，选取前3组赋分较高的工艺参数进行单层多道熔覆试验，测量单层多道熔覆层厚度及显微硬度，观察熔覆层金相组织，最后选出满足无磁发射短节熔覆层要求的工艺参数组合。

1.3　质量评价参数

裂纹密度、稀释率和成形系数是评价熔覆层质量的重要参数，现给出其计算公式便于后续使用。

裂纹密度表征的是裂纹敏感度，定义为单位长度内的裂纹数量[28]：

$$R_e = \frac{C}{L} \tag{1}$$

式中，R_e为裂纹密度，C为裂纹数，L为熔覆长度。

稀释率代表基体材料的熔化量，计算如下[29]：

$$\varphi = \frac{h}{H+h} \times 100\% \tag{2}$$

式中，φ为稀释率，H为熔高，h为熔深。稀释率过小，冶金结合效果就差，容易剥落；稀释率过大，则进入到熔覆层的基体成分较多，熔覆层有开裂倾向。

成形系数是一个综合考虑熔覆层宽度与基体熔化深度的参量，计算如下[29]：

$$\eta = \frac{W}{h} \tag{3}$$

式中，η为成形系数，W为熔宽。成形系数大，说明熔覆层的成形质量较为优异。

2　结果与分析

2.1　单层单道激光熔覆试验

16道单层单道Ni60合金熔覆层及其渗透探伤如图3所示。根据探伤裂纹数量计算的熔覆层裂纹率，测量熔覆层熔高H、熔宽W、熔深h、计算稀释率φ与成形系数η，具体数据见表4。

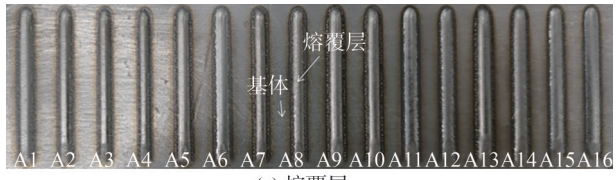

(a) 熔覆层

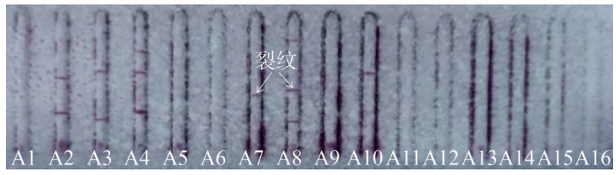

(b)裂纹探伤

图3　熔覆层及裂纹探伤

Fig. 3　Coatings and crack penetration

从图3可以看出，A2、A3、A4、A8熔覆层中含有较多的裂纹缺陷，A7和A10熔覆层也有少量裂纹缺陷。此外，A15、A16的稀释率过大(表4)，所以筛选出其余8组编号分别为A1、A5、A6、A9、A11、A12、A13、A14的熔覆层做进一步分析。筛选出的8组熔覆层横截面微观形貌如图4所示。由图4可知，熔覆层内部无明显裂纹、气孔等缺陷，成形良好。

表4 单层单道Ni60涂层横截面几何尺寸

Tab. 4 Cross section dimensions of single-layer single-pass Ni60 coatings

编号	裂纹密度 R_e/mm^{-1}	熔高 H/mm	熔深 h/mm	熔宽 W/mm	成形系数 η	稀释率 φ/%
A1	0	0.86	0.33	3.26	9.88	27.7
A2	0.050	0.96	0.07	3.06	43.71	6.8
A3	0.050	0.93	0.10	2.79	27.90	9.7
A4	0.075	0.99	0.07	2.54	36.29	6.6
A5	0	1.18	0.34	3.52	10.35	22.4
A6	0	0.71	0.33	3.39	10.27	31.7
A7	0.050	1.12	0.13	3.02	23.23	10.4
A8	0.075	0.76	0.05	2.95	59.00	6.2
A9	0	1.42	0.37	3.65	9.86	20.7
A10	0.025	1.26	0.27	3.46	12.81	17.6
A11	0	0.47	0.28	3.41	12.18	37.3
A12	0	0.59	0.23	3.40	14.78	28.0
A13	0	1.70	0.45	4.07	9.04	20.9
A14	0	1.12	0.41	3.80	9.27	26.8
A15	0	0.67	0.52	3.69	7.10	43.7
A16	0	0.30	0.57	3.82	6.70	65.5

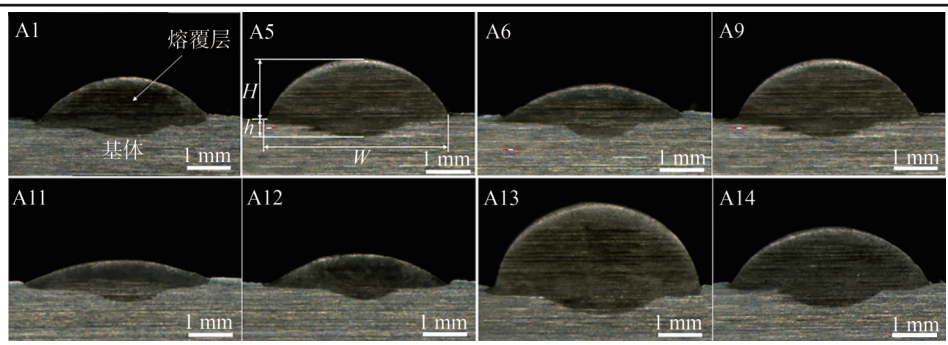

图4 筛选单层单道Ni60熔覆层横截面

Fig. 4 Cross sections of selected single-layer single-pass Ni60 coatings

裂纹产生原因与激光能量有关。因为激光功率、送粉量、扫描速度主要通过影响热输入从而影响熔覆层的开裂敏感性，所以当激光光斑直径固定时，工艺参数与激光能量的关系通常以线能量 E_L（$E_L=P/V_s$）和质能量 E_m（$E_m=P/V_t$）来表示[30]。图5为16组激光熔覆工艺参数下的激光线能量和质能量柱状图。从图5可以看出，A2、A3、A4、A7、A8组熔覆层的线能量及质能量水平均较低，虽然A10组的线能量不低，但其质能量仍处于一个较低的水平。当线能量较低时，单位时间内的熔覆层吸收激光能量变小，冷却速度变大，温度梯度变大，热应力增大，同时冷凝速度快会造成组织不均匀，开裂倾向增大。当质能量较低时，熔覆层吸收的能量低，合金粉末不能充分熔凝，在一定程度上也会造成组织不均匀，从而导致裂纹的产生。

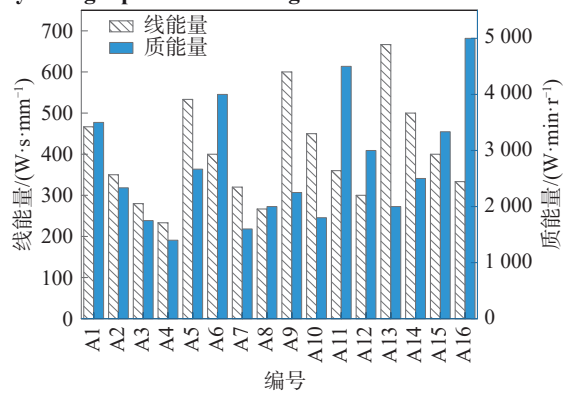

图5 不同工艺参数下的激光线能量和质能量

Fig. 5 Laser line energy and mass energy under different process parameters

利用显微维氏硬度计测量这8组熔覆层横截面的纵向显微硬度，即从熔覆层顶部向基体方向每间隔0.15 mm测量1次，其硬度分布如图6所示。由图6可以

看出，在不同激光熔覆工艺参数下，8组熔覆层基材硬度基本在205~232 HV之间，Ni60合金涂层硬度基本在528~788 HV之间。不同工艺参数下的Ni60熔覆层硬度略有不同，其中，A5组熔覆层的硬度最高，A6组熔覆层的硬度最低。结合表4的稀释率计算结果发现，熔覆层硬度与稀释率有较大关系，图7为8组熔覆层的平均显微硬度与稀释率的对应关系曲线。由图7可以看出，稀释率较大的A6和A11组的熔覆层硬度明显较低，这是因为当稀释率过大时，基体熔化较多，熔化的基体成分混入Ni60合金熔覆层，导致熔覆层中Fe含量增加，抑制了枝晶间硬质共晶组织的形成，造成了硬度的降低。

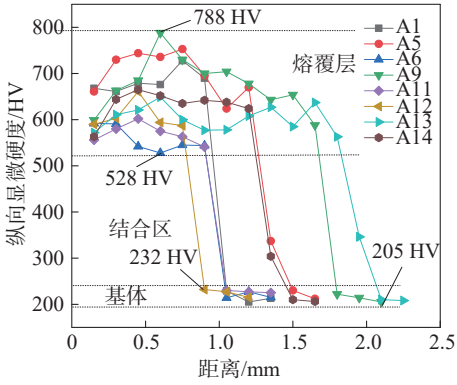

图6　筛选出的熔覆层纵向显微硬度

Fig. 6　Longitudinal microhardness of selected coatings

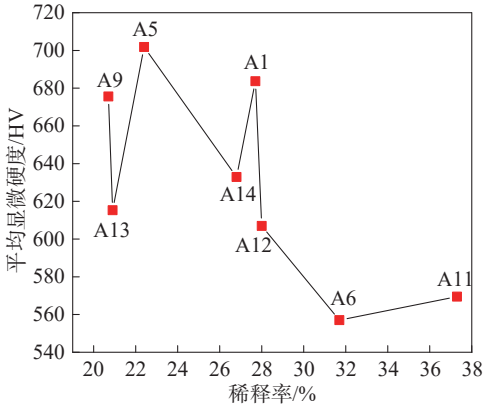

图7　熔覆层稀释率与硬度的关系

Fig. 7　Relationship between dilution rate and hardness of coatings

针对这8组熔覆层特性，以显微硬度、稀释率和成形系数为质量衡量指标，以高硬度、低稀释率、高成形系数为优，赋值硬度从低到高为1~8分，权重占比为50%；稀释率从高至低依次为1~8分，权重占比为30%；成形系数从低到高依次为1~8分，权重占比为20%，分别计算这8组熔覆层质量的综合加权得分，结果如图8所示。由图8可知，得分最高的熔覆层为A5（分数为7.0），其次为A9（分数为6.5），然后为A1（分数为5.0）。这3组熔覆层的共同点为稀释率较低，硬度较高，成形系数适中，因此综合加权分数较高。而A6和A11得分最低，分别为3.1分及3.7分，这两组熔覆层稀释率过高，硬度较低。因此，下一步将得分高的A1、A5、A9熔覆层的工艺参数作为优选工艺参数再进行单层多道熔覆试验。

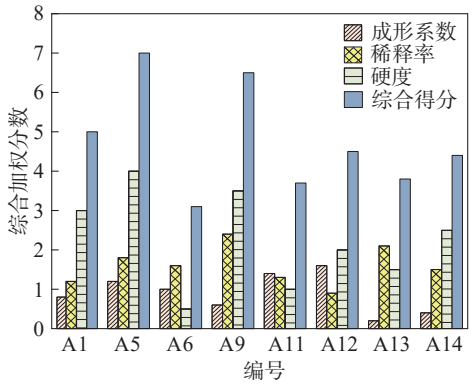

图8　8组熔覆层综合加权赋分

Fig. 8　Comprehensive weighted scores of 8 sets of coatings

2.2　单层多道激光熔覆试验

采用优选出的A1、A5、A9单层单道熔覆层的工艺参数，以50%搭接率和双向扫描路径制备出3组单层多道Ni60熔覆层，编号分别为G1、G2、G3，每组总道数为10，熔覆长度为40 mm，如图9所示。3组熔覆层的裂纹渗透探伤结果如图10所示。由图10可以看出，Ni60熔覆层表面形貌成形良好，无宏观裂纹缺陷。单层多道熔覆层的横截面形貌如图11所示。由图11可知，横截面无微观裂纹、孔洞等缺陷。

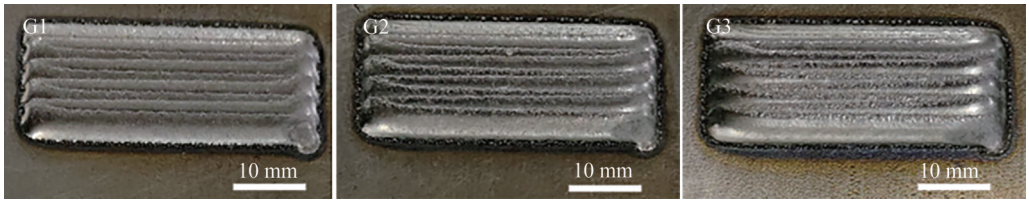

图9　3组单层多道熔覆层

Fig. 9　Three sets of single-layer multi-pass coatings

从图11可以看出，G1、G2、G3的熔覆层厚度逐渐增加，结合这3组熔覆层的加工工艺参数（表3）分析可发现：这3组工艺的激光扫描速度相同，而激光功率和送粉速率逐渐增加。增大激光功率提高了激光能量，而增大送粉速率则增加了合金粉末量，二者同时增加的情况下激光能量足够使粉末量充分熔凝，因此，熔覆层厚度会增加。

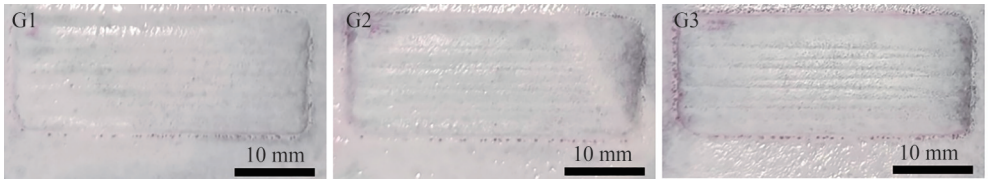

图 10 单层多道熔覆层裂纹探伤

Fig. 10 Crack penetrations of single-layer multi-pass coatings

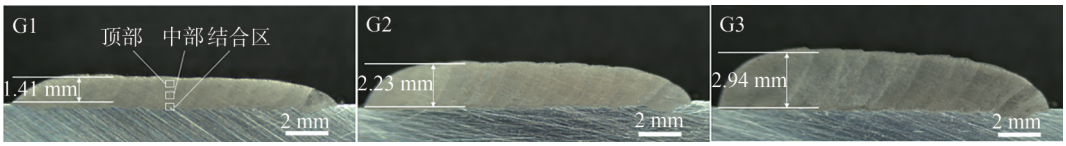

图 11 3 组单层多道熔覆横截面

Fig. 11 Cross sections of single-layer multi-pass coatings

通过测量横截面几何尺寸可得，G1 熔覆层在首道熔覆时稀释率为 30.9%，后续熔覆稀释率稳定在 17.8%~20.7% 之间；G2 熔覆层在首道熔覆稀释率为 26.3%，后续熔覆稀释率稳定在 15.3%~18.9% 之间；G3 熔覆层在首道熔覆稀释率为 22.8%，后续稀释率稳定在 7.6%~9.0% 之间。3 组熔覆层均在熔覆首道时出现了较大的稀释，后继道数的稀释率降低并逐渐平稳，主要原因是：在工艺初始时，激光能量通过粉末大量传输至基材，首道熔覆层出现了更深的激光穿透，在后续的熔覆中，由于轨道 50% 重叠，激光能量有部分作用于前一道熔覆材料，其余作用于本道熔覆层。比较而言，G3 熔覆层的稀释率最小，结合 3 组熔覆层的工艺参数可知，G3 熔覆层的送粉速率较大，粉末量较多，多数激光能量被粉末吸收，而基体吸收能量减小，因此，G3 熔覆层的稀释率较小。

在熔覆层横截面上使用显微维氏硬度计测量其硬度。首先，沿平行于基体方向测量 Ni60 合金涂层的横向硬度，每隔 1 mm 测量 1 次硬度，测量结果如图 12 所示。由图 12 可知，3 组涂层横向硬度最小为 588 HV，最大为 889 HV，且沿着熔覆方向硬度逐渐增大。然后，在熔覆层中宽处，沿垂直基体方向测量熔覆层的纵向硬度，从熔覆层顶部向基体方向每隔 0.15 mm 测 1 组硬度并取均值，测量结果如图 13 所示。由图 13 可以看出，Ni60 合金涂层硬度在 638~882 HV 之间，基体硬度在 218~273 HV 之间。Ni60 合金涂层的硬度可达 316L 不锈钢基体硬度的 4 倍左右，表面强化作用非常明显。

比较图 6 和 13 可以发现：相对于单层单道熔覆层，单层多道熔覆层硬度有所增加。这是因为多道熔覆层是每一道熔覆层以 50% 搭接率连接起来的，当前一道熔完再熔覆下一道时，由于激光热量高，相当于对前一道进行了二次熔融，使材料的晶粒再次细化，析出相的数量增多，因此，多道熔覆层硬度有所提高。

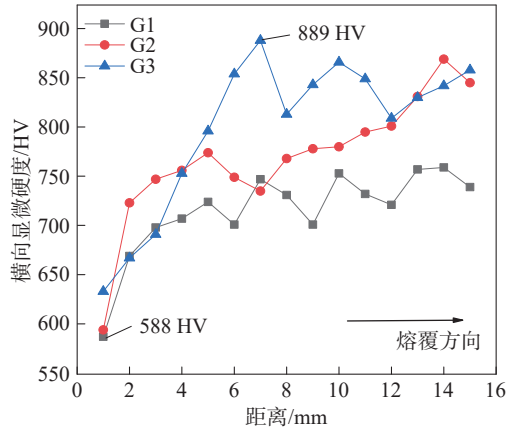

图 12 单层多道熔覆层横向硬度

Fig. 12 Lateral microhardness of single-layer multi-pass coatings

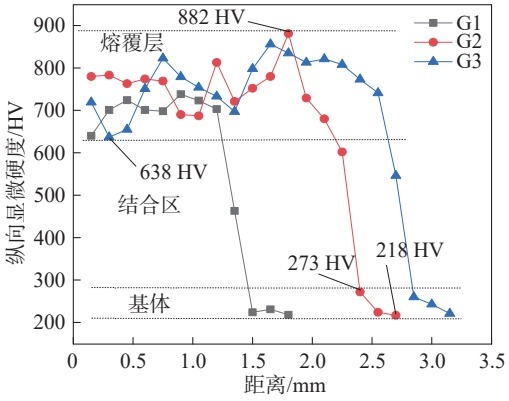

图 13 单层多道熔覆层纵向硬度

Fig. 13 Longitudinal microhardness of single-layer multi-pass coatings

良好成形的熔覆层除了宏观无裂纹和气孔，微观组织构成也要满足冶金结合条件。为了探究熔覆层微观组织的演变规律，按照图 11 中 G1 熔覆层标识的部位，采用倒置系统金相显微镜分别观察这 3 组熔覆层顶部、中部和结合区域的微观组织。图 14~16 分别为 G1、G2、G3 熔覆层的顶部、中部和结合区的金相组织形貌。从图 14~16 可以看出，3 组熔覆层的中、顶部区域金相组织由大量等轴晶和少量等轴树枝晶

组成。随着向结合区靠近，晶粒尺寸逐渐减小。其中，G1和G2熔覆层呈现了典型的快速凝固特征组织，即从结合区到熔覆层表面，组织形态呈现出从连续平面晶、树枝晶到等轴晶的转变（图14(c)、15(c)）。这是因为：在基体与熔覆层结合区，熔池底部热量通过基体快速导出，温度梯度最大方向近似垂直熔合线，因此，界面处热传导速度快、温度梯度大，在熔池底部温度的降低是均匀的，基本保持稳定的平面状，利于细小的平面晶生长；随着远离结合区，熔池温度梯度逐渐减小，熔覆层底部凝固前沿的溶质再分配使成分过冷增大，树枝晶在结合区上方区域生长，在凝固前继续推进至熔覆层表面，空气对流散热增加，熔池冷却速率增大，温度梯度继续减小，熔覆层中部、顶部区域微观组织以等轴晶及等轴树枝晶形状生长。平面晶薄层表面Ni60合金熔覆层与316L不锈钢基体形成了致密的冶金结合。而G3熔覆层结合区并未出现明显且连续的平面晶薄层（图16(c)），这与其熔覆时稀释率过低、在熔合处温度变化不均匀有关。

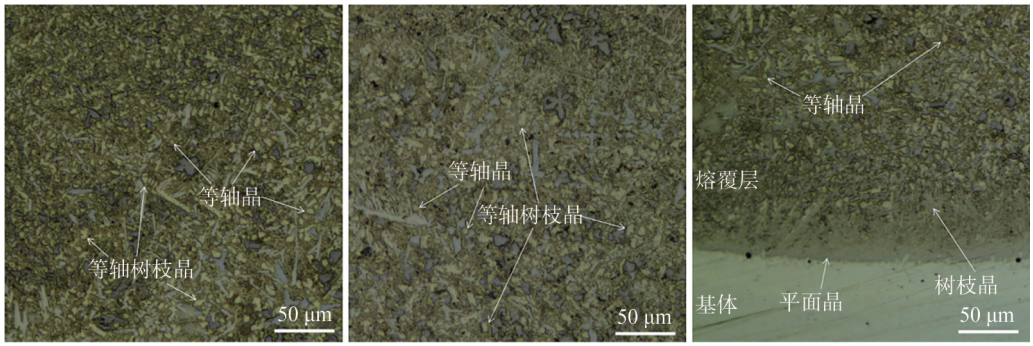

(a) 顶部　　(b) 中部　　(c) 结合区

图14　G1熔覆层金相组织

Fig. 14　Microstructure of G1 coating

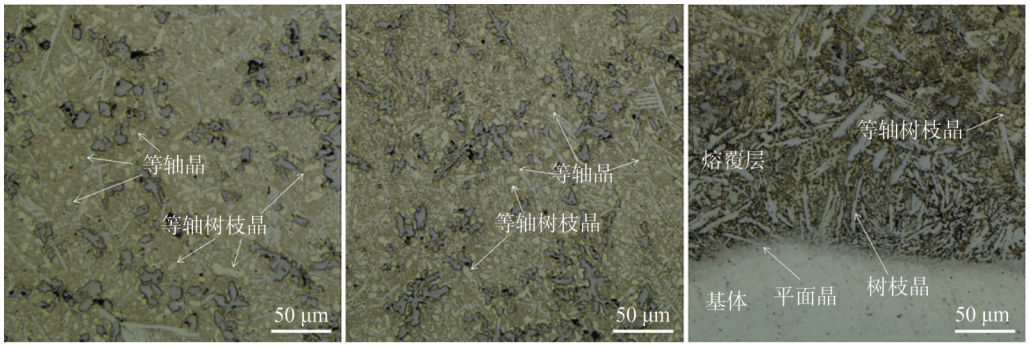

(a) 顶部　　(b) 中部　　(c) 结合区

图15　G2熔覆层金相组织

Fig. 15　Microstructure of G2 coating

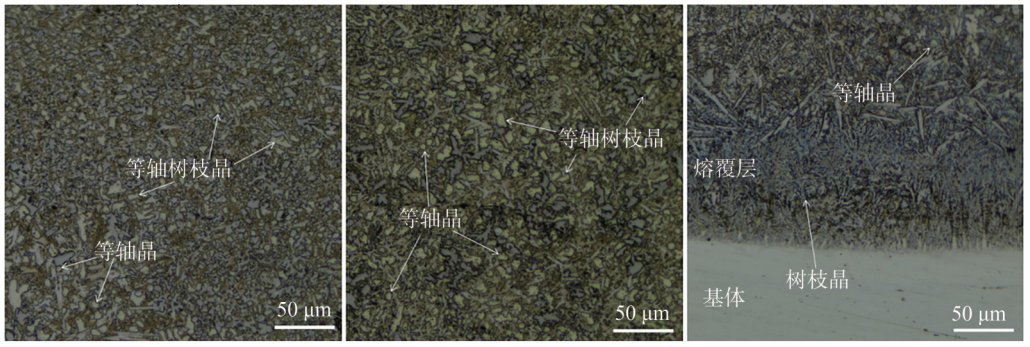

(a) 顶部　　(b) 中部　　(c) 结合区

图16　G3激光熔覆金相组织

Fig. 16　Microstructure of G3 coating

综上分析，G1和G2熔覆层均能满足无裂纹Ni60合金涂层制备要求。经测量，G1和G2熔覆层的平均厚度分别约为1.41 mm和2.23 mm（图11）。根据无磁发射短节对熔覆层厚度的要求可知，G2熔覆层满足厚度要求，且其硬度范围在691～882 HV区间，约为59.7～66.7 HRC，熔覆层硬度完全满足要求。因此，最

终确定G2熔覆层所对应的A5组工艺参数作为最佳使用参数，即：激光功率1 600 W，扫描速度3 mm/s，送粉速率0.6 r/min，搭接率50%。

3 结 论

本文通过激光熔覆正交试验及综合加权赋分方法获得了满足无磁钻具熔覆层制备要求的最佳工艺参数，所制备的熔覆层具有高硬度功能表面，冶金成形稳定，研究成果为解决无磁钻具磨损问题、延长其使用寿命提供了有效技术实现方案。主要结论如下。

1）在316L不锈钢表面开展单层单道激光熔覆Ni60合金粉末的正交试验。首先，筛选出无裂纹且满足稀释率的8组工艺参数组合；再以稀释率、成形系数和显微硬度为质量衡量指标进行综合加权赋分，得到3组优选工艺参数进行单层多道熔覆试验；最终，根据熔覆层显微硬度和金相组织得出满足无磁发射短节熔覆层厚度为2.0～2.5 mm、洛氏硬度在55～60 HRC的最佳工艺参数组合为激光功率1 600 W、扫描速度3 mm/s、送粉速率0.6 r/min、搭接率50%。

2）单层多道熔覆层的稀释率在首道较大，随着熔覆道数的增加稀释率逐渐减小并趋于平稳，稀释率在15%～20%时熔覆层微观组织形态从结合区到表面呈现出从连续平面晶、树枝晶到等轴晶的转变，无明显气孔、裂纹等缺陷，冶金成形良好。

3）单层多道Ni60合金涂层的横向显微硬度在熔覆初始相对较低，随着熔覆道数增加显微硬度逐渐增加并趋于稳定，范围在588～889 HV之间。在单层多道熔覆层的中宽处，熔覆层的纵向显微硬度在基体区域硬度较低，在结合区域硬度快速增大，到达Ni60合金涂层区域硬度最大，略有一定的波动。基体硬度在218～273 HV之间，Ni60合金涂层的纵向硬度在638～882 HV之间。Ni60合金熔覆层显微硬度可达316L基体硬度的4倍左右。

参考文献：

[1] Lin Xin, Yuan Renguo, Qin Lei, et al. Present situation and progress of geosteering drilling pre-prospecting technology[J]. Special oil & gas reservoirs, 2021, 28(2): 1–10. [林昕, 苑仁国, 秦磊, 等. 地质导向钻井前探技术现状及进展[J]. 特种油气藏, 2021, 28(2): 1–10.]

[2] Zong Xuewen, Yan Dan, Liu Wenjie, et al. Effect of annealing on wear characteristics and hardness of 316L stainless steel formed by SLM[J]. Applied Laser, 2022, 42(1): 31. [宗学文, 闫丹, 刘文杰, 等. 退火对SLM成形316L不锈钢磨损特性及硬度的影响[J]. 应用激光, 2022, 42(1): 31.]

[3] Feng Huanyin, Zhang Tao, Cai Liqing. Analysis of eccentric wear of non-magnetic tools for drilling tools[J]. Machine China, 2023(15): 53–56. [冯焕银, 张涛, 蔡黎清. 随钻仪器无磁工具偏磨使用分析[J]. 中国机械, 2023(15): 53–56.]

[4] Li Chao. Analysis on microstructure and properties of hardfacing wear belt for drill pipe joint[J]. Metallurgical Equipment, 2021, (2): 42–45. [李超. 钻杆接头堆焊耐磨带组织性能分析[J]. 冶金设备, 2021, (2): 42–45.]

[5] Xie Zihao, Liu Bo, Chao Yongli, et al. Research status and progress of laser cladding coatings on low carbon steel[J]. Metal Products, 2023, 49(4): 35–39. [谢子豪, 刘博, 晁永礼, 等. 低碳钢表面激光熔覆涂层研究现状及进展[J]. 金属制品, 2023, 49(4): 35–39.]

[6] Yan Zhongfang. Application of laser cladding technology on wear-resistant guide rail of drilling rig[J]. Coal Mine Machinery, 2022, 43(12): 159–160. [鄢忠方. 激光熔覆技术在钻机耐磨导轨上的应用[J]. 煤矿机械, 2022, 43(12): 159–160.]

[7] Yang Wenbin, Li Shiyu, Xiao Qian, et al. Research status and development trend of friction-reducing and wear-resistant laser cladding coatings[J]. Lubrication Engineering, 2023, 48(4): 171–182. [杨文斌, 李仕宇, 肖乾, 等. 减摩耐磨激光熔覆涂层的研究现状及发展趋势[J]. 润滑与密封, 2023, 48(4): 171–182.]

[8] Ya Wei, Pathiraj B, Matthews D T A, et al. Cladding of Trib-aloy T400 on steel substrates using a high power Nd:YAG laser[J]. Surface and Coatings Technology, 2018, 350: 323–333.

[9] Wang Lipeng, Zhang Dacheng, Chen Changzheng, et al. Multi-physics field coupling and microstructure numerical simulation of laser cladding for engine crankshaft based on CA–FE method and experimental study[J]. Surface and Coatings Technology, 2022, 438: 128396.

[10] Ding Haohao, Yang Tao, Wang Wenjian, et al. Optimization and wear behaviors of 316L stainless steel laser cladding on rail material[J]. Wear, 2023, 523: 204830.

[11] Ding Yuanhao, Dai Meng, Yao Xiaojiang. Application of wear belt technology in MWD instrument[J]. Instrumentation, 2022, 29(6): 31–33. [丁元皓, 代萌, 药晓江. 耐磨带技术在随钻仪器中的应用[J]. 仪器仪表用户, 2022, 29(6): 31–33.]

[12] Sorgato M, Bertolini R, Ghiotti A, et al. Tool wear assessment when drilling AISI H13 tool steel multilayered claddings[J]. Wear, 2023, 524: 204853.

[13] Tian Hongfang, Tantai Fanliang, Hou Qingling, et al. Research on the microstructure and propertiess of oil drill pipe prepared by laser additive manufacturing[J]. Thermal Spray Technology, 2018, 10(2): 75–82. [田洪芳, 澹台凡亮, 侯庆玲, 等. 石油钻杆激光增材制备耐磨带的组织结构及性能研究[J]. 热喷涂技术, 2018, 10(2): 75–82.]

[14] Man Guoxiang, Cheng Lin, Wang Kehu, et al. Technical analysis of wear belt of drill pipe[J]. Equipment for Geotechnical Engineering, 2021, 22(4): 3–6. [满国祥, 程林, 王

克虎,等.钻杆耐磨带技术分析[J].地质装备,2021,22(4):3–6.]

[15] Wei Ying, Wei Xianshun, Chen Bo, et al. Parameter optimization for tungsten carbide/Ni-based composite coating deposited by plasma transferred arc hardfacing[J]. Transactions of Nonferrous Metals Society of China, 2018, 28(12): 2511–2519.

[16] Li Dayan, Cui Xiufang, Yuan Chenfeng, et al. Effect of Ni modified graphene on microstructure and properties of Ni60 composite coatings prepared by laser cladding[J]. Optics & Laser Technology, 2021, 136: 106756.

[17] Liu Lilan, Li Sicong, Dou Weitao, et al. Process optimization and performance analysis for laser-cladding Ni60 alloy coating on surface of 316L stainless steel[J]. Chinese Journal of Lasers, 2024, 51(16): 1602207.[刘丽兰,李思聪,豆卫涛,等.316L不锈钢表面激光熔覆Ni60合金涂层的工艺优化与性能研究[J].中国激光,2024,51(16):1602207.]

[18] Lin Yinghua, Yuan Ying, Wang Liang, et al. Effect of electric–magnetic compound field on the microstructure and crack in solidified Ni60 alloy[J]. Acta Metallurgica Sinica, 2018, 54(10): 1442–1450.[林英华,袁莹,王梁,等.电磁复合场对Ni60合金凝固过程中显微组织和裂纹的影响[J].金属学报,2018,54(10):1442–1450.]

[19] Huang Haibo, Sun Wenlei. Influence of laser cladding process parameters on crack and thickness of Ni60[J]. Laser Technology, 2021, 45(6): 788–793.[黄海博,孙文磊.Ni60激光熔覆工艺参量对涂层裂纹及厚度的影响[J].激光技术,2021,45(6):788–793.]

[20] Wu Zupeng, Li Tao, Li Xiangbo. Effect of hybrid process parameters on crack behavior of laser cladding Ni60A alloy[J]. Applied Laser, 2019, 39(5): 765.[吴祖鹏,李涛,李向波.复合工艺参数对激光熔覆Ni60A合金裂纹的影响[J].应用激光,2019,39(5):765.]

[21] Li Qi, Li Tao, Wu Zupeng, et al. Study of crack mechanism in Ni-based alloy laser cladding coating[J]. Journal of Dalian University of Technology, 2020, 60(2): 159–164.[李琦,李涛,吴祖鹏,等.Ni基合金激光熔覆层裂纹机理研究[J].大连理工大学学报,2020,60(2):159–164.]

[22] Wang Yongdong, Zhang Yupeng, Zhang Ning, et al. Effect of Ni60A laser cladding process parameters on microstructure and properties of cladding layer[J]. Journal of Heilongjiang University of Science, 2021, 31(4): 446–451.[王永东,张宇鹏,张宁,等.激光熔覆工艺参数对Ni60A熔覆层组织及性能的影响[J].黑龙江科技大学学报,2021,31(4):446–451.]

[23] Wu Sha, Liu Zenghua, Huang Xiaofei, et al. Process parameter optimization and EBSD analysis of Ni60A–25% WC laser cladding[J]. International Journal of Refractory Metals and Hard Materials, 2021, 101: 105675.

[24] Liu Yu, Xu Tianhao, Li Guohui, et al. A multi-objective optimization of laser cladding process of Ni-based coating on the preheated copper alloy[J]. Materials Today Communications, 2023, 35: 105614.

[25] Shi Yameng, Li Jingbin, Zhang Jie, et al. Effect of process parameters on microstructure and wear resistance of 65Mn-based cladding Ni60a/SiC coating[J]. Journal of Mechanical Engineering, 2022, 58(16): 197–205.[史亚盟,李景彬,张杰,等.工艺参数对65Mn基熔覆Ni60a/SiC涂层的微观组织与耐磨性能影响[J].机械工程学报,2022,58(16):197–205.]

[26] Shi Qiang, Ma Xin, Bao Siqi, et al. Micro-structure and properties of high-speed laser cladding Ni60 coating on surface of high manganese steel[J]. Welding, 2023(11): 39–45.[史强,马欣,鲍思齐,等.高锰钢表面高速激光熔覆Ni60涂层组织与性能[J].焊接,2023:39–45.]

[27] Wang Qian, Chen Faqiang, Li Qian, et al. Microstructure and properties of Ni60 alloy coating prepared by electromagnetic compound field assisted laser cladding[J]. Materials Chemistry and Physics, 2022, 291: 126678.

[28] Ma Min. Research on state identification of cladding layer in metal laser cladding process[D]. Dalian: Dalian University of Technology, 2022.[马敏.金属激光熔覆过程熔覆层的成形状态识别研究[D].大连:大连理工大学,2022.]

[29] Peng Yaojun, Zhang Jianlin, Li Yuhang, et al. Process optimization, microstructure and properties of laser–cladded stellite6 coatings[J]. Applied Laser, 2023, 43(2): 11–19.[彭耀军,张建林,李宇航,等.激光熔覆Stellite6涂层工艺优化及组织性能研究[J].应用激光,2023,43(2):11–19.]

[30] Gao Xun. Study on composition and technology of laser cladding Ni60 powder[D]. Shijiazhuang: Shijiazhuang Tiedao University, 2019.[高珣.激光熔覆Ni60粉末的成分及工艺研究[D].石家庄:石家庄铁道大学,2019.]

Research on the Process of Ni60 Laser Cladding for Surface Strengthening of Nonmagnetic Drilling Tools

LIU Lilan[1], *LI Sicong*[1], *YANG Fan*[1], *HAN feiyan*[2], *WU Ziying*[1]

(1.School of Mechanical and Precision Instrument Engineering, Xi'an University of Technology , Xi'an 710048, China;
2.School of Aeronautical Manufacturing Engineering, Xi'an Aeronautical Polytechnic Institute, Xi'an 710089, China)

Abstract:

Objective The material of nonmagnetic drilling tools is 316L stainless steel. When operating underground, nonmagnetic drilling tools are prone to wear and corrosion due to the poor wear and corrosion resistance of 316L stainless steel. Cladding a carbide alloy on the surface of

nonmagnetic drilling tools serves as an effective method to enhance their wear and corrosion resistance. Ni60 alloy exhibits high hardness and wear resistance; however, it also presents high crack sensitivity, which seriously restricts its engineering application. This study aims to determine the optimal process parameters for preparing crack-free Ni60 alloy coatings on 316L stainless steel substrates to strengthen the surface of nonmagnetic drilling tools.

Methods Laser coaxial powder feeding technology was utilized to clad Ni60 alloy powder on the surface of 316L stainless steel. The process parameters, such as laser power, scanning speed, and powder feeding rate, were considered as influencing factors. First, orthogonal experiments of single-layer single-pass laser cladding were conducted. Sixteen sets of single-layer single-pass cladding layers were obtained, and penetration testing was employed to detect cracks in the cladding layers. An inverted metallographic microscope was then utilized to observe the microstructures of the cross-sections of the cladding layers, and a Vickers hardness tester was utilized to measure the microhardness of the cladding layers. The melting height, melting depth, and melting width of the 16 sets of single-layer single-pass cladding layers were measured to calculate the crack density, dilution rate, and forming coefficient. Some cladding layers with no cracks and a low dilution rate were selected from the 16 sets. Next, taking microhardness, dilution rate, and forming coefficient as quality indicators, a comprehensive weighted scoring method was proposed to select three sets of cladding layers with the highest scores. The process parameters of the selected three sets of single-layer single-pass cladding layers were then utilized to conduct single-layer multi-pass cladding tests with a 50% overlap rate. The microhardnesses and microstructures of the single-layer multi-pass cladding layers were measured. Based on the thickness, microstructure, and microhardness of the single-layer multi-channel cladding layers, the process parameters that met the requirements of the coatings for the nonmagnetic drilling tool considered were finally determined.

Results and Discussions In the results of the single-layer single-pass cladding experiments, crack defects were found in the cladding layers of A2, A3, A4, A7, A8, and A10. The laser energy analysis showed that their line energy and mass energy were low, which led to incomplete melting of the alloy powder and also caused the microstructures of the layers to be uneven. In addition, the cladding layers of A15 and A16 were also eliminated because their dilution rates were too high. The remaining eight sets of cladding layers, which exhibited no cracks or pores in their cross-sections, were selected for further analysis. The hardness of the Ni60 alloy coating ranged from 528 to 788 HV, while the hardness of the substrate ranged from 205 to 232 HV. Taking microhardness, dilution rate, and forming coefficient as quality evaluation indicators, with high hardness, low dilution rate, and high forming coefficient considered optimal, the comprehensive weighted scores of the selected eight sets of single-layer single-pass cladding layers were calculated. The three sets of cladding layers with the highest scores were A5, A9, and A1, and their process parameters were utilized to conduct single-layer multi-channel experiments. Therefore, three sets of single-layer multi-channel cladding layers, numbered G1, G2, and G3, were obtained. The crack penetration testing showed that there were no cracks in the cladding layers. The thicknesses of the G1, G2, and G3 cladding layers gradually increased due to the corresponding increases in laser power and powder feeding rate. The dilution rate of the G1 cladding layer remained between 17.8% and 20.7%, that of G2 remained between 15.3% and 18.9%, and that of G3 remained between 7.6% and 9.0%. The microhardness of the Ni60 alloy coating ranged from 638 to 882 HV, and the hardness of the substrate ranged from 218 to 273 HV. The microstructures of the G1 and G2 cladding layers exhibited typical rapid solidification characteristics. From the bonding zone to the surface of the cladding layers, the microstructures showed a transition from continuous planar crystals and dendritic crystals to equiaxed crystals. This illustrated that the Ni60 alloy powder formed a dense metallurgical bond with the 316L stainless steel substrate. However, no obvious and continuous planar crystal layer was found in the bonding zone of the G3 cladding layer, which was attributed to the low dilution rate and uneven temperature variation.

Conclusions The Ni60 alloy coating of the G2 cladding layer meets the requirements of a 2.0～2.5 mm thickness and a 55～60 HRC hardness for the nonmagnetic drilling tool. When the dilution rate is approximately 15%～20%, the microstructure of the single-layer multi-channel cladding layer exhibits good formation without cracks or pores. The transverse microhardness of the single-layer multi-channel Ni60 alloy coatings ranges from 588 to 889 HV. At the middle width of the single-layer multi-channel cladding layer, the longitudinal microhardness of the Ni60 alloy coating ranges from 638 to 882 HV, while the longitudinal microhardness of the 316L substrate ranges from 218 to 273 HV. The microhardness of the Ni60 alloy coating is approximately four times that of the 316L substrate. The optimal process parameters, determined through experiments and analysis, are as follows: laser power of 1 600 W, scanning speed of 3 mm/s, powder feeding rate of 0.6 r/min, and overlap rate of 50%.

Key words: nonmagnetic drillings; Ni60 alloy; comprehensive weighted scoring; process optimization

（编辑　吴芝明）

引用格式: Liu Lilan,Li Sicong,Yang Fan,et al.Research on the process of Ni60 laser cladding for surface strengthening of nonmagnetic drilling tools[J].Advanced Engineering Sciences,2025,57(4):303–312.[刘丽兰,李思聪,杨帆,等.面向无磁钻具表面强化的Ni60合金激光熔覆工艺研究[J].工程科学与技术,2025,57(4):303–312.]